Polymer Testing 164 (2026) 109381

Contents lists available at ScienceDirect

Polymer Testing

journal homepage: www.elsevier.com/locate/polytest

Multiscale Fingerprinting of a Disruption–Recombination Crossover in Cyanate Ester Networks under Extreme Neutron Irradiation

Minjung Han [a,1], Kisu Kim [a,1], Gyeongjun Kim [b,1], Youngsu Jeong [d,1], Hyunjun Lee [a], Wonjin Na [e,f], Min Wook Lee [g], Dae Han Sung [h], Ki-Ho Nam [i,j], Hyeonuk Yeo [j,k], Jaegi Lee [d,*], Hyeong Min Jin [b,c,**], Youngho Eom [a,***]

[a] Department of Organic and Nano Engineering, Human-Tech Convergence Program, Hanyang University, 222 Wangsimni-ro, Seoul, 04763, Republic of Korea
[b] Department of Organic Materials Engineering, Chungnam National University, 99 Daehak-ro, Yuseong-gu, Daejeon, 34134, Republic of Korea
[c] Department of Materials Science and Engineering, Chungnam National University, 99 Daehak-ro, Yuseong-gu, Daejeon, 34134, Republic of Korea
[d] HANARO Utilization Division, Korea Atomic Energy Research Institute (KAERI), 111 Daedeok-daero 989beon-gil, Yuseong-gu, Daejeon, 34057, Republic of Korea
[e] Composite Materials Application Research Center, Korea Institute of Science and Technology (KIST), 92 Chudong-ro, Bongdong-eup, Wanju-gun, Jeollabuk-do, Republic of Korea
[f] Department of JBNU-KIST Industry-Academia Convergence Research, Jeonbuk National University, 567 Baekje-daero, Deokjin-gu, Jeonju-si, Jeollabuk-do, Republic of Korea
[g] Institute of Advanced Composite Materials, Korea Institute of Science and Technology, Jeonbuk, 55324, Republic of Korea
[h] Mechanical and Aerospace Engineering, Utah State University, Logan, Utah, 84322, USA
[i] Department of Textile System Engineering, Kyungpook National University, Daegu, 41566, Republic of Korea
[j] School of Chemical Engineering and Applied Chemistry, Kyungpook National University, Daegu, 41566, Republic of Korea
[k] Department of Chemistry Education, Kyungpook National University, Daegu, 41566, Republic of Korea

ARTICLE INFO

Keywords:
Cyanate ester
Neutron irradiation
Multiscale analysis
Structural aging

ABSTRACT

The growing use of radiation-durable cyanate ester (CE) thermosets in aerospace systems and radiation-intensive facilities demands analytical approaches capable of resolving hidden aging mechanisms and supporting lifetime prediction. Here, we establish a multiscale fingerprinting framework that correlates characteristic irradiation-induced signatures across mechanical, macroscopic, microscopic, nano-/subnanometer, and molecular scales. Over an accelerated absorbed dose range of 0–6.2 MGy, the CE network exhibits two distinct aging regimes separated at approximately 2.1 MGy, rather than simple monotonic degradation. In the low-dose regime, chemical alteration and partial cleavage of methylene and aromatic ether linkages promote radical formation, network loosening, free-volume expansion, and a decrease in surface modulus from 5.7 ± 0.4 to 5.1 ± 0.6 GPa. At higher doses, radical recombination and secondary crosslinking become dominant, leading to partial restoration of linkage-related chemical environments, network densification, free-volume contraction, and modulus recovery to 6.0 ± 0.4 GPa. Notably, optical imaging, SEM, and SAXS provide little evidence of this mechanistic transition, whereas PALS, WAXS, XPS, gradient-mapped FTIR, and nanoindentation yield distinct and mutually consistent dose-dependent fingerprints. Their cross-scale correlation identifies the transition dose and reveals that neutron-induced aging is governed primarily by molecular and nano-/subnanometer structural evolution without pronounced microscale morphological damage. This fingerprinting framework provides a rational basis for detecting hidden radiation damage and assessing the long-term durability of radiation-resistant thermosetting networks. Nevertheless, further validation across different CE formulations and radiation environments is required to establish the broader applicability of the identified transition behavior.

* Corresponding author.
** Corresponding author.
*** Corresponding author.
E-mail addresses: jgl@kaeri.re.kr (J. Lee), hyeongmin@cnu.ac.kr (H.M. Jin), eomyh@hanyang.ac.kr (Y. Eom).
[1] These authors contributed equally to this work.

https://doi.org/10.1016/j.polymertesting.2026.109381
Received 9 August 2026; Received in revised form 18 September 2026; Accepted 5 October 2026
Available online 6 October 2026
0142-9418/© 2026 The Authors. Published by Elsevier Ltd. This is an open access article under the CC BY license (http://creativecommons.org/licenses/by/4.0/).

1. Introduction

Cyanate ester (CE) resins are high-performance thermosetting polymers widely utilized as matrix resins and electrical insulation materials in advanced aerospace structures and radiation-intensive facilities [1,2]. During thermal curing, the cyanate (–O–C ≡ N) groups undergo cyclotrimerization to form six-membered cyanurate (1, 3, 5-triazine) rings, producing a densely crosslinked polycyanurate network [3,4]. This network architecture provides the cured resins with excellent thermomechanical and dielectric properties, including a high glass-transition temperature (T_g > 250 °C), low dielectric loss, low moisture absorption, and high dimensional stability [5,6]. Due to these attributes, CE-based materials are promising candidates for maintaining structural integrity and functional performance under harsh thermal and radiation environments [7,8].

Despite their densely crosslinked structures, however, CE-based materials are not completely resistant to radiation-induced aging. For example, gamma (γ)-irradiated CE/benzoxazine networks showed an initial reduction in flexural properties, T_g, storage modulus, and thermal stability at 250 kGy, followed by partial recovery at 500 kGy and a slight decline at 1000 kGy [9]. In CE/epoxy blend systems exposed to γ-ray doses of up to 100 MGy, decomposition of ether linkages was accompanied by decreases in T_g and flexural strength [8]. These findings demonstrate that radiation exposure can alter the chemical structure, network organization, thermal stability, and mechanical performance of CE-based thermosets, despite their inherent resistance to severe environments.

Radiation-induced aging of polymer networks involves multiple competing reactions, including bond scission, oxidation, radical recombination, and additional crosslinking [10–14]. The relative contributions of these reactions depend on the chemical structure and network architecture of the materials, as well as irradiation parameters such as radiation type, absorbed dose, dose rate, temperature, and atmosphere [10,12,15]. Owing to the complexity of these competing processes, various characterization techniques have been employed to evaluate irradiation-induced changes in mechanical and thermal properties, chemical structure, and morphology [7–9,16,17]. However, most studies have focused on isolated post-irradiation responses or the overall extent of property deterioration. Accordingly, it remains difficult to determine how damage initiates and propagates across different length scales, whether the dominant aging mechanism changes with absorbed dose, and which analytical responses most sensitively capture such a transition. A multiscale fingerprinting approach that extracts and correlates characteristic dose-dependent signatures across complementary structural levels is therefore required to distinguish competing irradiation-induced processes.

Here, we establish a multiscale analytic framework to elucidate the structural aging of CE networks over an accelerated absorbed dose range of 0–6.2 MGy (Fig. 1). Macroscopic responses were assessed using optical appearance observation and ultraviolet-visible (UV–Vis) spectroscopy, while microscopic surface morphology was examined by scanning electron microscopy (SEM) and atomic force microscopy (AFM). At the subnanometer and nanometer levels, positron annihilation lifetime spectroscopy (PALS), small-angle X-ray scattering (SAXS), and wide-angle X-ray scattering (WAXS) were employed to characterize the evolution of free volume, network heterogeneity, and molecular organization. These structural responses were correlated with molecular- and chemical-level changes identified by Fourier-transform infrared (FTIR) spectroscopy and X-ray photoelectron spectroscopy (XPS), as well as local mechanical responses measured by microscratch and nanoindentation tests. In this study, a "multiscale fingerprint" is operationally defined as a set of correlated, dose-dependent analytical signatures such as changes in trend, onset, or inflection behavior that consistently indicate a transition in the dominant aging response across different structural length scales. By comparing these signatures, we identify the analytical indicators that most sensitively resolve changes in the dominant aging mechanism and distinguish absorbed-dose-dependent degradation regimes. This fingerprinting framework therefore provides a mechanistic basis for durability assessment and, ultimately, lifetime prediction under extreme radiation conditions.

2. Experimental

2.1. Materials

A commercial CE resin system based on Primaset® PT-30 and Primaset® BA-3000 was supplied by Arxada Ltd. (Switzerland). PT-30 is a multifunctional phenolic-novolac-based CE resin, while BA-3000 is a bisphenol-A-based CE resin. A cobalt-based curing catalyst predispersed in YDPN-638 novolac epoxy resin was provided by Kukdo

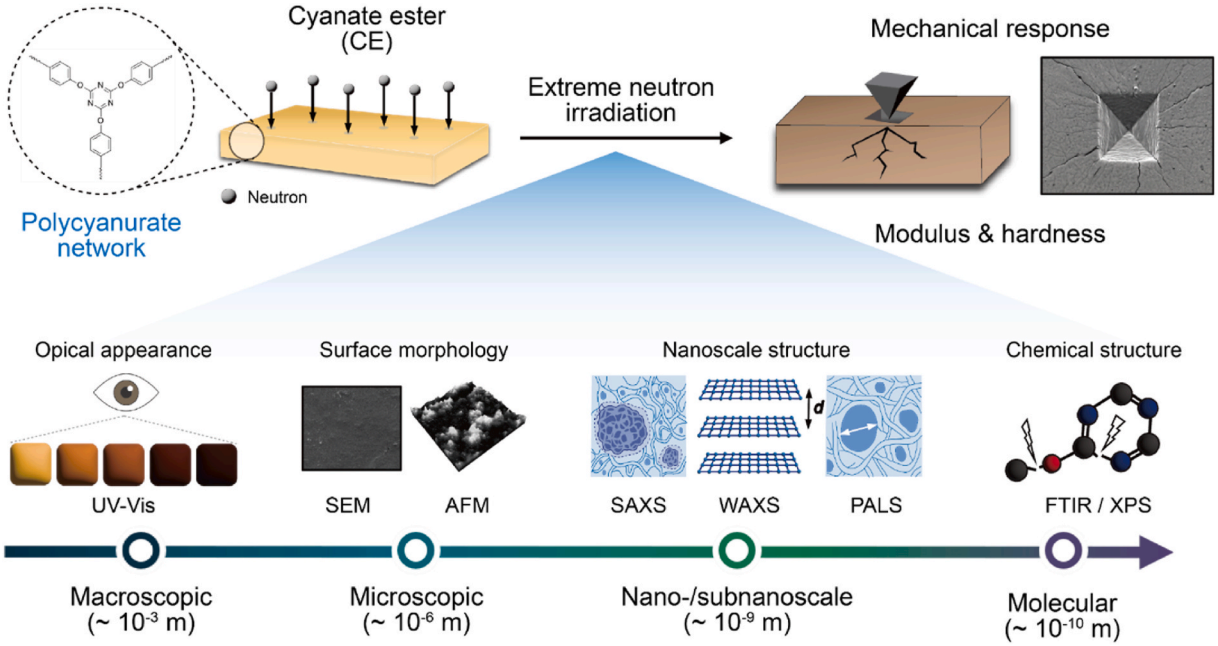

Fig. 1. Schematic overview of the multiscale characterization framework for neutron-irradiated CE networks.

Chemical Co., Ltd. (Republic of Korea). The CE resin system and the catalyst dispersion were mixed at a supplier-recommended mass ratio of 100:5, corresponding to a cobalt concentration of approximately 0.1 ppm in the final resin formulation. All materials were used as received without further purification.

2.2. Preparation of CE specimen

An open-ended aluminum mold containing bar-shaped cavities of 12.7 × 60.0 × 1.0 mm^3 was placed on an aluminum plate without a mold-release agent. The resin was poured into the mold and degassed in a vacuum oven at 100 °C for 1 h under a gauge pressure of approximately −0.10 MPa. The resin-filled mold was subsequently transferred to a furnace preheated to 175 °C and cured in air for 3 h. After curing, the furnace was switched off, and the specimens were allowed to cool naturally to room temperature inside the furnace. The cured bars were demolded and cut into 10 × 10 × 1 mm^3 for neutron irradiation, with the cutting positions determined using ImageJ.

2.3. Neutron irradiation of CE specimen

For each exposure time, four specimens were loaded into a separate high-density polyethylene rabbit (22.5 mm outer diameter, 57.9 mm high, 11.97 cm^3 free volume, melting point 131.6 °C), which was flushed with nitrogen and then vented by a 1.1 mm hole through the capsule wall to relieve the pressure transients of pneumatic transfer and to release radiolytic gases (Supplementary Note 1). The rabbit was transported and irradiated inside the transfer line, which is filled with nitrogen of 99.998% purity; nitrogen rather than air is used in this system to suppress $^{40}Ar(n, \gamma)^{41}Ar$ activation [18]. However, the capsules were not hermetically sealed, and the residual oxygen concentration was not measured; therefore, the irradiation atmosphere should not be regarded as completely oxygen-free. Accelerated total ionizing dose testing of polymers is usually performed with cobalt-60 (Co-60) γ-ray sources, electron beams, or proton beams. In this study, a research reactor γ-field was used for two reasons. First, its dose rate is two to three orders of magnitude higher than that of a conventional Co-60 facility, allowing megagray-level doses to be achieved within hours rather than weeks. Second, the field is highly penetrating, providing a spatially uniform dose distribution throughout the specimen thickness, in contrast to electron- and proton-beam irradiation, which deposit energy with a depth gradient.

Irradiation was performed in the NAA-2 vertical hole of the HANARO research reactor at the Korea Atomic Energy Research Institute, operated at a thermal power of 27 MW, using a pneumatic transfer system with nitrogen as the carrier gas (Supplementary Note 2). Specimens were exposed for 1, 2, 4, and 6 h. The absorbed dose rate in the resin was estimated to be 285 Gy s^{-1}, corresponding to total ionizing doses of approximately 1.0, 2.1, 4.1 and 6.2 MGy, respectively. This estimate was derived by scaling published calorimetric measurements of nuclear heating in this reactor [19] to the hole used in the present study, based on reported thermal neutron fluxes [18], and converting from aluminum to the resin matrix using the ratio of mass energy absorption coefficients. The resulting exposure is a mixed neutron–γ field, in which γ-rays account for 94% of the absorbed dose, and the $^{14}N(n, p)^{14}C$ reaction on nitrogen within the resin accounts for the remaining 6%. The derivation and its assumptions are provided in the Supplementary Note 2.1. The irradiation temperature was not monitored directly. The temperature of this irradiation hole has, however, been measured during facility commissioning with irreversible thermal indicators attached to capsules of the same type, giving 60–65 °C for irradiation times of 1–3.6 h at 30 MW. Scaled to the 27 MW operating power used here and corrected for the 4.7 K difference between the specimens and the capsule wall, the specimen temperature was estimated to be approximately 65–70 °C. An independent conduction-and-radiation heat balance provided a conservative upper bound below 95 °C (Supplementary Note 2.2). Consistent with this estimate, the capsules, with a measured melting point of 131.6 °C, showed no softening or distortion after 6 h of irradiation. The thermal time constant of the assembly was approximately 5 min, which is substantially shorter than the irradiation durations. Therefore, the specimens were expected to approach comparable quasi-steady temperatures after the initial heating period and to remain more than 180 K below the glass transition temperature of the cured resin.

2.4. Characterization

The surface morphologies of the neutron-irradiated CE resin specimens were examined using a field-emission SEM (FE-SEM, S-4800, Hitachi, Japan) without conductive coating. All specimens were imaged at an accelerating voltage of 1 kV under identical conditions. SEM images were further analyzed using ImageJ. For each SEM image, 10 line profiles were drawn at different positions across the image, and the standard deviation (SD) of gray values was calculated for each line as an image-based descriptor of pixel-intensity variability. Three-dimensional (3D) intensity maps were also generated to visualize the spatial distribution of gray values (Fig. S1). The vertical axis of these maps represents image intensity rather than physical surface height.

Surface roughness was examined using AFM (Cypher S, Asylum Research, Oxford Instruments, USA) in tapping mode. Height-retrace images were acquired from three independently selected regions for each irradiation condition. The arithmetic mean roughness was calculated using the Asylum Research analysis software.

SAXS and WAXS measurements were performed using a NANOPIX instrument (Rigaku, Japan) equipped with a micro-focus Cu rotating-anode X-ray generator [20–22]. Cu Kα radiation (λ = 1.5418 Å) was used at an X-ray power of 1.2 kW. SAXS and WAXS patterns were collected at sample-to-detector distances of 1350 and 97 mm, with exposure times of 600 and 300 s, respectively. The two-dimensional (2D) scattering images were converted into one-dimensional (1D) intensity profiles using 2DP software, and the profiles were processed using Igor Pro 6.37 and Origin 2024. No additional background subtraction was performed during post-processing. The final scattering profiles are presented over a q range of approximately 0.004-2.4 $Å^{-1}$. For SAXS analysis, the low-q power-law slope was evaluated over q = 0.005–0.014 $Å^{-1}$. For WAXS analysis, the broad amorphous halo was fitted using a Gaussian function to determine the halo position (x_c) and full width at half maximum (FWHM). The characteristic intermolecular spacing was calculated as (Eq. (1)) [20]:

$$d = \frac{2\pi}{x_c} \tag{1}$$

The FWHM of the fitted halo was used to compare changes in the distribution of local amorphous packing environments. In addition, the high-q region at q = 2.2–2.4 $Å^{-1}$ was compared using identically processed WAXS profiles to evaluate changes in local short-range structural correlations.

Free-volume characteristics were analyzed using PALS at the Korea Atomic Energy Research Institute (KAERI, Republic of Korea). $A^{22}Na$ positron source was prepared on a 7.6-μm-thick polyimide film and sandwiched between two identical specimens. For each specimen, a lifetime spectrum containing at least 4.0 × 10^6 counts was acquired. The spectra were analyzed using *PALSfit3* after source correction, and the lifetime components, $_{\tau i}$, and normalized intensities, $_{Ii}$, were obtained [23]. The longest lifetime component, $_{\tau 3}$, was assigned to ortho-positronium annihilation in free-volume holes [24]. PALS measurements were performed approximately 55 days after irradiation, by which time induced activity had decayed and residual radical concentrations had substantially relaxed, so that quenching of ortho-positronium by trapped radicals does not contribute significantly to the reported I_3 values. The mean free-volume hole radius was calculated using the Tao–Eldrup model with ΔR = 0.17 nm [25,26], and the relative fractional free-volume parameter was estimated from the

free-volume hole size and I_3.

Optical properties were evaluated using a UV–Vis–NIR spectrophotometer (Cary 5000, Agilent Technologies, USA) in transmission mode over 200–800 nm. Specimens with thicknesses of approximately 1 mm were used. The absorption coefficient was calculated from the measured transmittance and specimen thickness, and the apparent direct optical band gap was estimated from Tauc plots, $(\alpha h\nu)^2$ versus $h\nu$ [27].

XPS was performed using a K-Alpha + spectrometer (Thermo Scientific, USA) equipped with a monochromatic Al Kα X-ray source [28,29]. The X-ray spot size was 400 μm. Survey spectra were acquired with a pass energy of 200 eV and an energy step size of 1.0 eV. High-resolution spectra were collected with a pass energy of 50 eV and an energy step size of 0.1 eV for the C 1s, O 1s, and N 1s regions. Charge compensation was applied using a dual-beam low-energy electron/Ar^+ ion charge neutralizer. The binding-energy scale was charge-corrected by setting the C 1s hydrocarbon peak to 284.8 eV. Peak fitting was performed using Thermo Scientific Avantage software, and the fitted spectra were plotted using OriginPro 2024. A Shirley-type Smart background was used for background subtraction. The high-resolution spectra were deconvoluted using Gaussian–Lorentzian product functions with a GL(30) line shape.

Chemical-structure changes were examined using an attenuated total reflectance (ATR)-FTIR spectrometer (Nicolet iS50, Thermo Fisher Scientific, USA). Spectra were collected over 4000–600 cm^{-1} at a resolution of 4 cm^{-1} by averaging 64 scans. The spectra were baseline-corrected using identical manually selected anchor points and area-normalized over the same wavenumber range. Dose-dependent spectral variations were visualized using 2D gradient maps calculated from the numerical derivative of the area-normalized absorbance with respect to nominal absorbed dose [30,31].

ESR spectroscopy was performed to examine residual radical species in the irradiated CE specimens. Powdered CE specimens were placed in ESR sample tubes, and spectra were collected at room temperature using an X-band ESR spectrometer (JES-X320, JEOL, Japan). The spectra were acquired at a microwave frequency of 9448.848 MHz, microwave power of 0.998 mW, field center of 336.000 mT, sweep width of ±15.000 mT, sweep time of 30 s, modulation frequency of 100.00 kHz, and modulation width of 0.2000 mT. The first-derivative ESR signal near g ≈ 2.00

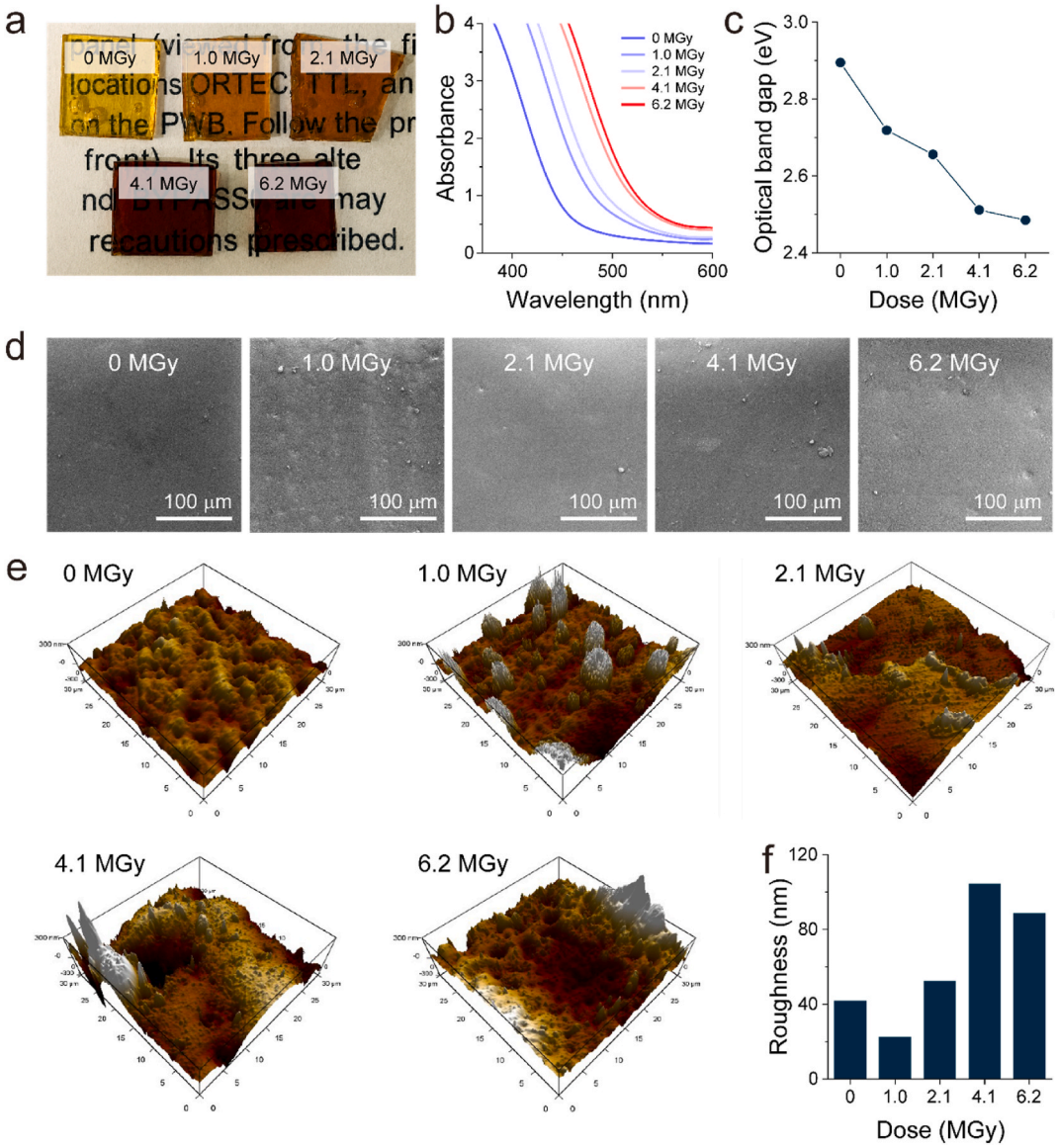

Fig. 2. Optical and surface morphological evolution of neutron-irradiated CE network. (a) Photographs showing progressive discoloration at 0, 1.0, 2.1, 4.1, 6.2 MGy. (b) UV–Vis absorption spectra and (c) apparent optical band gap as a function of irradiation dose. (d) Surface SEM images, (e) AFM topography images, and (f) corresponding surface roughness.

was compared as a function of absorbed dose.

Microscratch tests were performed using the MCT module of a Step 500 scratch-testing platform (Anton Paar, Austria) with a Rockwell C diamond indenter. Each test consisted of a pre-scan, a 3-mm progressive-load scratch from 10 mN to 5000 mN, and a post-scan. The elastic recovery ratio was calculated from the penetration depth during scratching and the residual depth after unloading. The resulting scratch tracks were additionally examined by optical microscopy.

Nanoindentation tests were performed using the NHT3 nanoindentation module installed on the same Step 500 platform and equipped with a spherical diamond indenter with a radius of 20 μm. The tests were performed at room temperature under load-controlled conditions with a constant indentation strain rate of 0.1 s^{-1} up to a maximum load of 75 mN. The indentation modulus, EIT, and hardness, HIT, were determined from the load–displacement curves using the Oliver–Pharr method [32,33].

3. Results and discussion

3.1. Macroscopic-to-microscopic analysis: discoloration and surface morphology

Among the multiscale analyses spanning macroscopic to molecular levels, the effect of accelerated neutron irradiation on the CE specimens was first evaluated visually from their macroscopic optical appearance (Fig. 2a). With increasing the absorbed dose from 0 to 6.2 MGy, the specimens progressively changed from bright yellow to dark brown and became increasingly opaque, indicating the accumulation of radiation-induced damage. Yellowing is one of the most common manifestations of aging in polymeric materials exposed to various types of radiation [7,34]. Similar discoloration has also been observed in irradiated cyanate-based materials and has been associated with radiation-induced reactions involving aromatic groups and oxidative degradation, leading to the formation of conjugated species and oxidation products [35]. UV–Vis spectroscopy quantitatively confirmed these optical changes, showing a red shift in the absorption cut-off and increased absorption in the visible-light region of 400–700 nm with increasing absorbed dose (Fig. 2b) [16,36–38]. In addition, the progressive decrease in the optical band gap from 2.9 to 2.5 eV after irradiation suggests the formation of radiation-induced chromophores and localized electronic states that enable lower-energy electronic transitions (Fig. 2c) [38,39]. The monotonic decrease in the apparent optical band gap with increasing absorbed dose also suggests its potential as a measurable optical indicator of radiation exposure. Such a dose-dependent response could be exploited for radiation dosimetry or sensor design in mixed-radiation environments, as well as for in-situ monitoring of radiation-induced damage in CE-based components [40]. However, such applications would require dedicated calibration and validation under representative mixed-radiation conditions.

From a microscopic perspective, the surface morphology of the CEs was examined using SEM and AFM (Fig. 2d and e). Despite the visually evident and progressive discoloration, the SEM images revealed negligible irradiation-induced damage at the microscale, such as surface cracking, erosion, or defect formation (Fig. 2d). To quantitatively assess changes in SEM image texture, the gray-value standard deviation (SD) was calculated as an image-based surface-texture descriptor (Fig. S1a) [41,42], together with the corresponding 3D intensity maps (Fig. S1b). The gray-value SD represents the degree of pixel-intensity variation within the analyzed regions and may reflect differences in image texture. Neither the gray-value SD nor the 3D intensity maps exhibited a systematic dependence on absorbed dose, indicating no clear dose-dependent change in the surface texture. Consistently, AFM topographic images obtained from more localized surface regions showed no distinct morphological changes attributable to neutron irradiation (Fig. 2e). Although the surface roughness varied from 22.4 to 104.3 nm (Fig. 2f), it exhibited no monotonic dose dependence. This variation is more likely associated with the intrinsic surface heterogeneity and pre-existing local defects, rather than with irradiation-induced roughening. Unlike atomic oxygen, which directly causes oxidative erosion of exposed polymer surfaces, neutrons and γ-rays do not preferentially deposit energy at the surface [43–45]. Their more penetrating interactions can therefore induce extensive chemical and structural changes throughout the material without necessarily producing discernible surface erosion. These macroscopic-to-microscopic observations indicate that the pronounced optical discoloration was not accompanied by detectable surface erosion, but was primarily associated with nanoscale and molecular-level phenomena.

3.2. Nano-to-subnanometer-scale analysis: free volume and molecular packing

To probe neutron-induced structural changes at smaller length scales, PALS spectra were first employed to examine the subnanometer free-volume structure of the CE network. PALS provides key structural parameters describing the average size and effective population of free-volume holes. Among the resolved lifetime components, the longest lifetime component, τ_3, corresponds to the annihilation of ortho-positronium (o-Ps) confined within free-volume holes [25,26]. Because o-Ps survives longer in a larger empty space, τ_3 reflects the average size of the free-volume holes. The average hole radius (R) was calculated from τ_3 using the Tao–Eldrup model. In contrast, I_3, the relative intensity of the o-Ps component, is associated with the effective population or accessibility of free-volume sites available for o-Ps formation [24,46]. The fractional free volume (FFV) was subsequently estimated by combining the hole volume derived from R with I_3.

In contrast to the larger-scale analyses, the PALS results revealed two distinct dose-dependent regimes (Fig. 3a and b). In the low-dose region up to 2.1 MGy, τ_3 and the corresponding R increased slightly, from 1.76 ± 0.01 ns and 2.62 ± 0.01 Å for the unirradiated specimen to 1.79 ± 0.01 ns and 2.65 ± 0.01 Å for the irradiated specimen, respectively (Fig. 3a). This behavior suggests that neutron irradiation initially enlarged the average size of the free-volume holes, likely through local chain scission and structural relaxation within the CE network [10,11,46]. In contrast, I_3 decreased moderately over the same dose range, from 22.07 ± 0.15% to 19.36 ± 0.20%, indicating a gradual reduction in the effective population or accessibility of o-Ps-detectable free-volume sites (Fig. 3b). Given the opposite trends in τ_3 and I_3, the low-dose response is better understood as a redistribution toward fewer, or less accessible, but slightly larger free-volume holes rather than as a simple increase in the total free volume. Because the increase in hole size partly compensated for the decrease in I_3, the FFV remained nearly unchanged in this region (Fig. 3b).

A contrasting behavior was observed above 2.1 MGy. In the high-dose region, τ_3 and R decreased with increasing absorbed dose, while I_3 continued to decline (Fig. 3a and b). Consequently, the FFV decreased markedly, reaching 2.49 ± 0.05% at 6.2 MGy, compared with 2.99 ± 0.04% for the unirradiated specimen. The simultaneous decreases in R, I_3, and FFV indicate that the free-volume holes became both smaller and less accessible at high absorbed doses. This trend suggests progressive densification of the CE network, which may be attributed to radical recombination, chain rearrangement, and additional crosslinking. A comparable free-volume contraction was reported for γ-irradiated epoxy, where the mean hole volume decreased from 0.113 to 0.091 nm^3 and the fractional free volume decreased from 1.711 to 1.217% between 0 and 861.84 kGy [47]. The authors attributed these reductions to irradiation-induced free-radical reactions and increased crosslinking, which reduced the intermolecular space available for positronium formation. This behavior is qualitatively consistent with the high-dose contraction observed in CE. However, unlike the predominantly decreasing free-volume response of the irradiated epoxy, CE initially exhibited slight free-volume-hole enlargement before contraction at higher absorbed doses, indicating a distinct dose-dependent

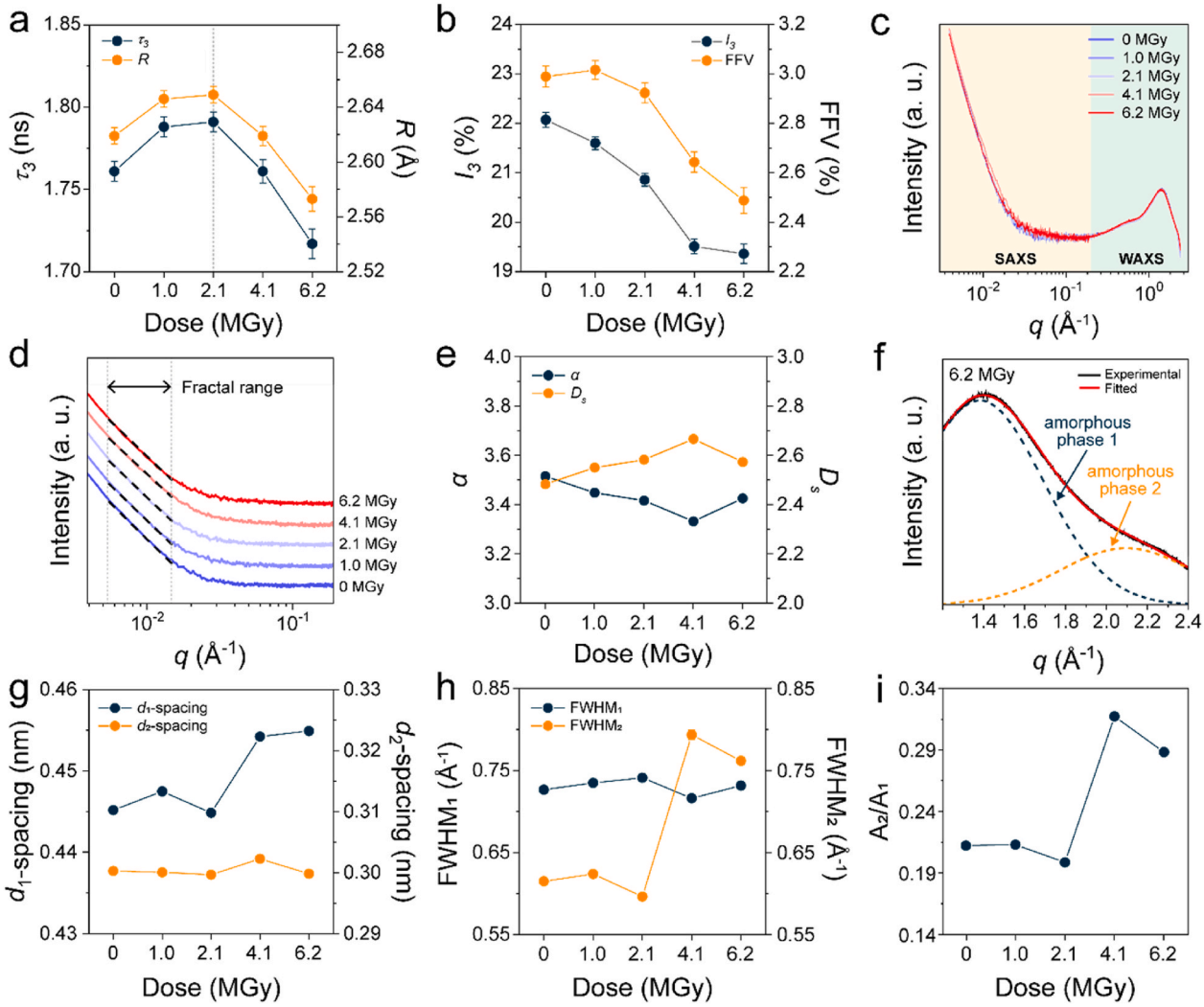

Fig. 3. Nanoscale structural evolution of cured CE network after neutron irradiation. (a) PALS-derived τ_3 and R. (b) I_3 and FFV. (c) Combined SAXS/WAXS profiles over the full q-range. (d) SAXS profiles in the fractal range. (e) α and D_s. (f) Representative deconvolution of the WAXS profile at 6.2 MGy into two amorphous phases. Irradiation-induced changes in (g) d-spacings, (h) FWHMs, and (i) A_2/A_1 of the two amorphous phases.

crossover from local network loosening to compaction.

To determine whether the free-volume changes extended to larger length scales and to investigate their relationship with molecular packing, complementary SAXS and WAXS analyses were performed. The scattering profiles exhibited a monotonic decrease in intensity in the low-q SAXS region, and a broad amorphous halo centered at $q \approx 1.4$ Å^{-1} at all absorbed doses (Fig. 3c). No new correlation peaks or crystalline diffraction features emerged with increasing dose, indicating that the overall nanoscale morphology and amorphous character of the CE network were largely retained without pronounced phase separation or crystallization. Changes in the low-q SAXS region were quantified using the power-law exponent, α, and the corresponding surface fractal dimension, $D_s = 6 - \alpha$ (Fig. 3d). The marginal variations in both α and D_s across the entire dose range indicate that neutron irradiation induced only minor changes in interfacial roughness and did not substantially reorganize the nanoscale structure (Fig. 3e).

In contrast, WAXS revealed distinct dose-dependent changes in short-range molecular packing. Although the broad amorphous halo centered at $q \approx 1.4$ Å^{-1} was retained for all samples (Fig. 3f), the scattering intensity in the high-q region of q = 2.2–2.4 Å^{-1} increased noticeably for the high-dose specimens. Deconvolution of the broad halo into correlation components identified a dominant amorphous phase 1 with a characteristic distance (d_1-spacing) ≈ 0.445 nm and a weaker short-range phase 2 with a characteristic distance (d_2-spacing) ≈ 0.300 nm (Fig. 3g). The former is attributed to average inter-segmental packing within the amorphous polycyanurate network, whereas the latter is tentatively assigned to short-range local atomic correlations involving the aromatic and cyanurate units at a length scale of approximately 3 Å [48,49]. In the low-dose region of 0–2.1 MGy, the d-spacing and FWHM values for both phases remained nearly unchanged (Fig. 3g and h). This negligible variation in molecular packing is consistent with the nearly constant FFV obtained from the PALS analysis. In other words, although local chain scission and structural relaxation may have occurred, these changes did not appreciably disturb the average short-range packing of the triazine and aromatic units.

At higher dose ranges, however, d_1-spacing increased sharply to 0.454 nm, while the $FWHM_2$ increased markedly to 0.79 ± 0.01 Å^{-1} at 4.1 MGy (Fig. 3g and h). The increase in d_1-spacing indicates relaxation of the average inter-segmental packing associated with phase 1, potentially arising from accumulated linkage damage and chain scission. Meanwhile, the increase in the $FWHM_2$ suggests that the local structural environment associated with the aromatic units became increasingly heterogeneous, even though the average d_2-spacing remained nearly unchanged. Notably, the substantial increase in the integrated-area ratio of phase 2 to phase 1, A_2/A_1, at higher doses indicates an increased relative contribution of the more compact short-range correlation in

phase 2 (Fig. 3i). These apparently contrasting changes suggest heterogeneous structural reorganization at high doses: some regions of the network become locally relaxed because of accumulated bond scission, whereas other regions develop more compact short-range packing through radical recombination and re-crosslinking [10].

Irradiation-induced changes in nanoscale structure have also been examined by SAXS and WAXS in electron-irradiated Kapton polyimide [50]. In that study, a broad SAXS feature associated with a characteristic length scale of approximately 10 nm disappeared after irradiation, while wide-angle diffraction peaks associated with the backbone repeat distance and preferential chain packing decreased in intensity. These observations were interpreted as a disruption of pre-existing molecular order accompanying irradiation-induced chemical changes. By comparison, the CE network retained its overall SAXS profile and amorphous WAXS halo, despite changes in the deconvoluted short-range correlations at higher doses. Thus, the two polymers exhibited different scattering responses to irradiation. This comparison should be interpreted qualitatively because both the initial network structures and irradiation conditions differ.

Overall, neutron irradiation did not substantially alter the nanoscale morphology of the CE resin but induced a distinct dose-dependent reorganization of its subnanometer structure. The complementary PALS and WAXS results consistently indicate that local chain scission and structural relaxation dominate at low doses, whereas radical recombination, re-crosslinking, and heterogeneous molecular repacking become increasingly important at higher doses.

3.3. Molecular-level analysis: chemical bonding and functional groups

XPS analysis was performed to examine the neutron-irradiation-induced changes in the chemical bonding environment of the CE network (Fig. 4 and Table S1). In the C 1s spectra, the C=C/C–C component decreased from 96.8% to 90.3% with increasing absorbed dose, whereas the C–O/C–N component increased from 3.2% to 8.0% (Fig. 4a). High-binding-energy components assigned to C=O and O–C=O/O–C=N emerged at 2.1 MGy, and the O–C=O/O–C=N contribution increased to 1.7% at 4.1 MGy. Consistent changes were observed in the O 1s spectra: the relative contribution of backbone oxygen, including ether and aromatic C–O environments, decreased from 95.8% to 90.4%, while the C–OH/O–C=O component increased from 4.2% to 7.2% (Fig. 4b). A high-binding-energy O 1s component associated with O=C–OH/H_2O was also detected from 2.1 MGy onward. Together, the C 1s and O 1s results indicate that irradiation progressively reorganizes the bonding environment around the polymer backbone through oxidation. The N 1s spectra exhibited a more distinct change in the high-dose regime (Fig. 4c). While only the triazine nitrogen component (triazine N, C–N=C) at approximately 398.7 eV was observed for low-dose CEs (0–2.1 MGy), a new high-binding-energy component appeared at approximately 400 eV, accounting for 15.3% of the total N 1s area at 4.1 MGy. This component, assigned to an oxidized or oxygen-influenced nitrogen environment, increased to 18.7% at 6.2 MGy, while the triazine nitrogen contribution decreased to 84.7% and 81.3%, respectively. These results show that the nitrogen environment around

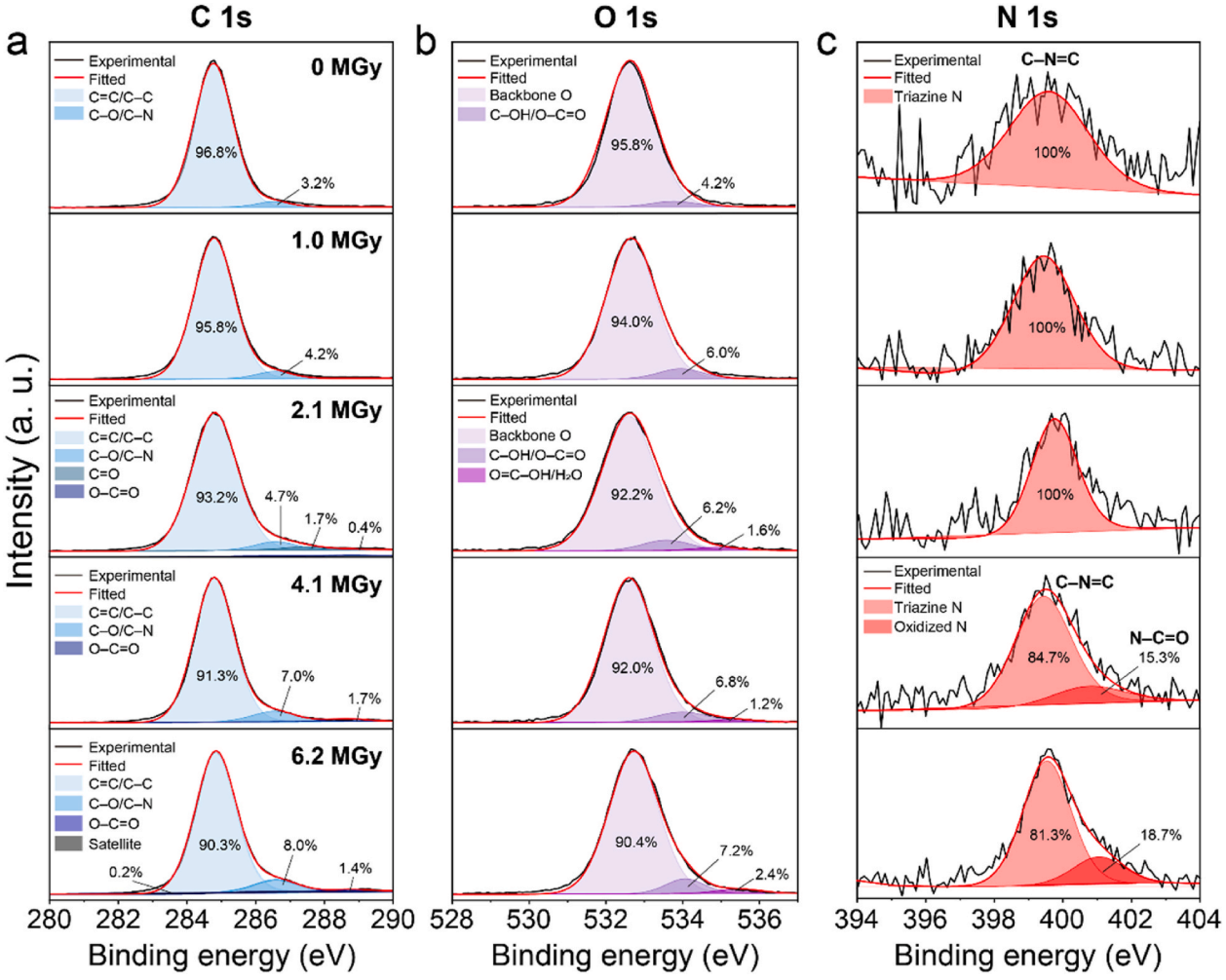

Fig. 4. XPS analysis of neutron irradiation-induced surface chemical changes in CE resins. Deconvoluted high-resolution (a) C 1s, (b) O 1s, and (c) N 1s spectra of CE specimens irradiated at nominal absorbed doses of 0–6.2 MGy.

the triazine rings or their adjacent linkages is evidently affected by the recombination mechanism of the free radical components at high-dose range, rather than the chain scission at low-dose range.

Previous irradiation studies of CE systems have reported different XPS responses depending on resin chemistry and exposure conditions. Wang et al. [51] observed an increase in the C–C/C–H contribution in γ-irradiated PEGDGE-modified CE, whereas Peng and Han [52] reported an increased C–C contribution for CE exposed to electron irradiation under high vacuum. In contrast, the present neutron-irradiated CE exhibited a decreasing C=C/C–C contribution accompanied by increasing oxygen-containing components. These contrasting trends likely reflect differences in network composition, radiation type, and irradiation environment, which alter the relative contributions of bond degradation, recombination, and formation of oxidized species. In addition, the decrease in ether-related O 1s environments observed here is consistent with the preferential susceptibility of ether linkages

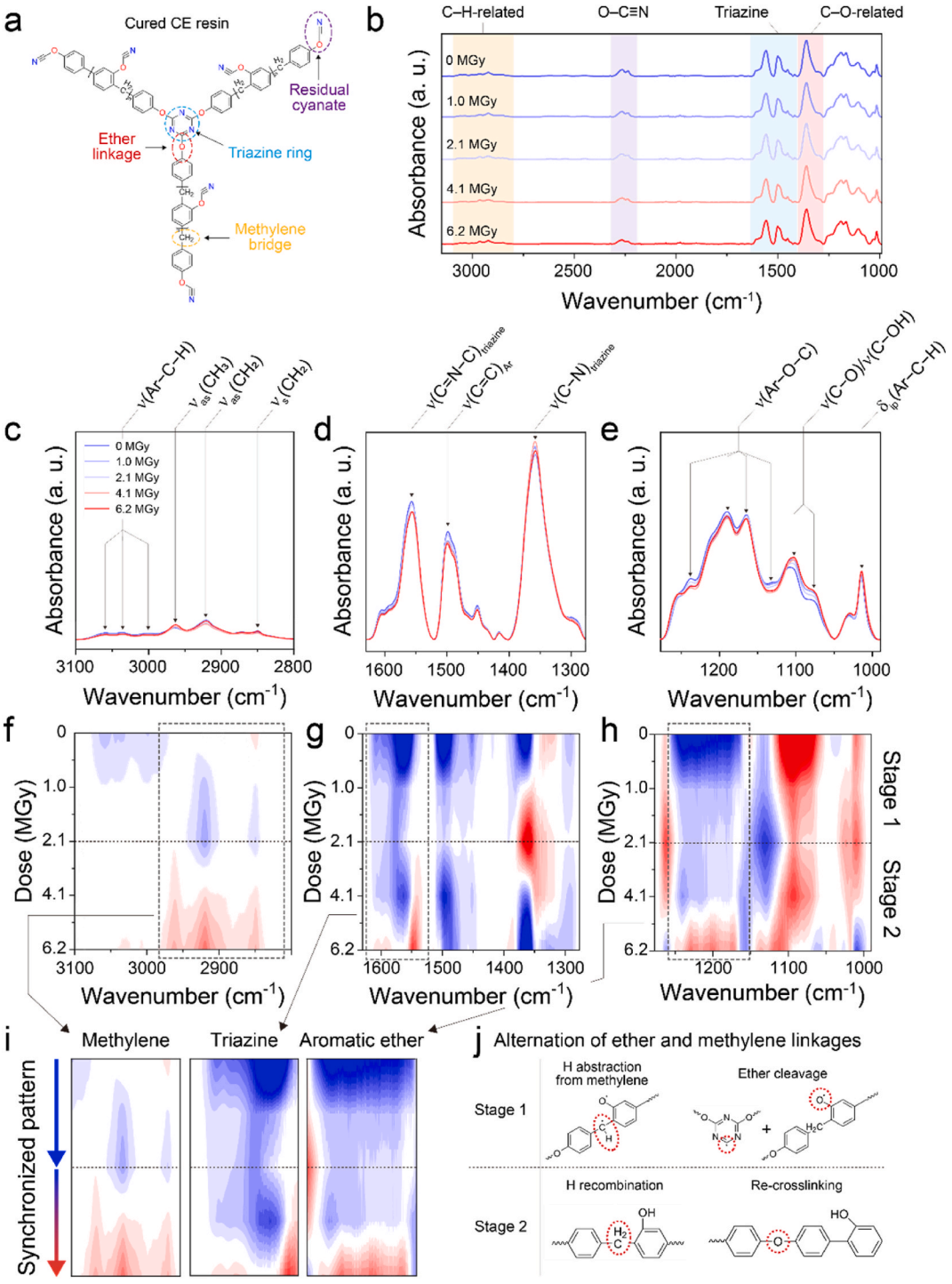

Fig. 5. FTIR analysis of neutron irradiation-induced chemical changes in the cured CE network. (a) Representative cured CE structure highlighting the major bonding environments. (b) FTIR spectra over the full wavenumber range. Enlarged spectra of the (c) C–H stretching region (3100–2800 cm^{-1}), (d) triazine-related region (1630–1277 cm^{-1}), and (e) C–O-related region (1277–990 cm^{-1}), and (f-h) corresponding 2D gradient maps. (i) Synchronized gradient patterns of representative methylene, triazine, and aromatic ether bands. (j) Schematic illustration of representative reactions associated with the two-stage neutron irradiation response.

previously reported for γ-irradiated CE/epoxy systems [8]. Taken together with the other multiscale analyses, the XPS results suggest that the low-dose regime is dominated by bond disruption, whereas the emergence of new oxygen- and nitrogen-containing chemical environments at higher doses is consistent with increasingly pronounced network reorganization and radical recombination.

Irradiation-induced alterations in the chemical structure were further examined by FTIR analysis (Fig. 5). The cured CE network can be mainly described in terms of four structural motifs: triazine units, ether and other oxygen-containing linkages, methylene linkages, and residual cyanate groups (Fig. 5a) [1,3,53]. In the 1D FTIR spectra, these motifs are represented by bands in the ranges of 3100–2800 cm^{-1} (C–H-related vibrations), 2315–2215 cm^{-1} (cyanate groups), 1630–1277 cm^{-1} (triazine-related vibrations), and 1277–990 cm^{-1} (C–O-related vibrations) (Fig. 5b and Fig. S2a) [3,54,55]. The absence of pronounced changes in the 1D spectra indicates that neutron irradiation does not cause extensive destruction of the crosslinked CE network. Instead, it appears to induce relatively subtle alterations in the more irradiation-sensitive linkages within the network.

To resolve these subtle spectral variations more clearly, 2Dgradient maps were constructed [30,31]. These maps visualize the dose-dependent variations in band absorbance, and thus provide insight into how individual chemical bonds respond to increasing neutron exposure. The maps were generated from the first derivative of absorbance (A) with respect to absorbed dose, expressed as dA/dMGy, in the MGy (y-axis) versus wavenumber (x-axis) space (Fig. 5f–h and Fig. S2b). Red and blue contours represent positive and negative dA/dMGy values, corresponding to increases and decreases in A with increasing dose, respectively. First, the consistent blue contour of ν(O–C ≡ N) band near 2250 cm^{-1} indicates the gradual consumption of residual cyanate groups during irradiation, possibly through secondary reactions with hydroxyl- or epoxy-derived species (Fig. S2b). In addition, the distinct red contour assigned to ν(C–O)/ν(C–OH) suggests a progressive increase in oxygen-containing chemical components, which is consistent with the XPS results (Fig. 5e–h).

In contrast to these monotonic variations, nonmonotonic dose-dependent responses were clearly observed in three spectral regions associated with methylene linkages, ether linkages, and triazine units. These regions are examined in greater detail in Fig. 5i. They showed a similar response: their band absorbances initially decreased (blue contours) in the low-dose regime, but subsequently increased (red contours) in the high-dose regime. Ether and methylene linkages are generally more susceptible to irradiation-induced reactions than the highly crosslinked triazine units [8]. This difference has been attributed to the representative bond-dissociation energies of 530 kJ mol^{-1} for C–O, compared to 745 kJ mol^{-1} for C–N bonds. In the low-dose regime, the blue contours of the bands associated with the two linkages suggest hydrogen abstraction from the methylene groups and partial cleavage or chemical alteration of the aromatic ether linkages. These reactions are expected to generate carbon-centered and oxygen-centered radical species within the CE network (Fig. 5j). Above 2.1 MGy, on the other hand, the transition from negative to positive gradient maps suggests the partial restoration or reformation of these chemical structures through radical recombination, secondary crosslinking, and hydrogen-transfer reactions [10,11,51].

Interestingly, the triazine-related spectral region at 1650−1500 cm^{-1} exhibited a synchronized dose-dependent pattern with those of the linkages (Fig. 5i). This behavior suggests that the spectral response of the triazine units is strongly influenced by structural changes in their surrounding linkages, rather than by extensive decomposition of the triazine rings themselves. Nevertheless, partial rearrangement, tautomerization, or secondary functionalization of the triazine units may also occur, as evidenced by WAXS and XPS analyses. Consequently, the 2D gradient FTIR analysis reveals that neutron irradiation progressively promotes oxidation while mainly inducing a nonmonotonic structural response in the ether and methylene linkages of the CE network. In particular, the competition between these degradation and recombination pathways, as visualized by the 2D gradient maps, is therefore considered a primary origin of the dose-dependent structural evolution of the irradiated CE network.

To further examine the involvement of radical species, ESR spectroscopy was performed as a supplementary validation experiment (Fig. S3). A first-derivative ESR signal at g ≈ 2.00 increased with absorbed dose, supporting the formation and dose-dependent increase of long-lived paramagnetic species in the irradiated CE network [56,57]. Together with the nonmonotonic FTIR response, this result supports a radical-mediated structural evolution involving competing bond disruption and network reorganization. Because ESR detects residual radicals after irradiation rather than transient recombination events, radical recombination is considered a plausible contributor to the high-dose structural and mechanical recovery rather than a directly observed process. Nonetheless, the contribution of residual oxygen to the observed oxidative changes cannot be determined quantitatively because the residual oxygen concentration inside the capsules was not measured and the capsules were not hermetically sealed. In addition, post-irradiation exposure to air may have contributed to the measured chemical state.

3.4. *Multiscale fingerprinting of the dose-dependent transition in the aging mechanism*

The irradiation-induced structural evolution, particularly at the nano-/subnanometer and molecular levels, was reflected in the local mechanical response of the CE network. Fig. 6 presents the surface mechanical properties of the CE specimens evaluated by microscratch and nanoindentation tests. The microscratch tracks and elastic-recovery profiles showed negligible variations with increasing absorbed dose (Fig. 6a and b). The largely preserved scratch resistance demonstrates that the CE network maintains its microscale mechanical durability even at high absorbed dose. At the smaller length scale probed by nanoindentation, however, the mechanical response exhibited a distinct dose dependence (Fig. 6c–e). In the low-dose regime of 1.0−2.1 MGy, the load–displacement curves shifted toward greater penetration depths, indicating decreases in indentation modulus and hardness (Fig. 6c–e). This mechanical deterioration can be attributed to the loosening of the crosslinked network. The interpretation is supported by the partial cleavage and chemical alteration of methylene/ether linkages at the molecular level, together with the accompanying expansion of the free-volume structure at the subnanometer level. In the high-dose regime above 2.1 MGy, the mechanical properties recovered, with the highest modulus and hardness observed at 4.1 MGy. This recovery indicates the restiffening and densification of the damaged network. The reversed mechanical response is consistent with the partial restoration of the methylene/ether-related chemical bonds via radical recombination and secondary crosslinking, followed by contraction of the free-volume structure.

Comprehensive analysis of the multiscale responses reveals that the irradiated CE network evolves through two distinct dose-dependent regimes rather than undergoing simple monotonic degradation. The characteristic signatures obtained from each analytical method, which serve as multiscale fingerprints for identifying the dominant mechanisms in the dose regimes, are summarized in Fig. 7a. Optical imaging, SEM, and SAXS did not reveal a clear transition between the two regimes, whereas PALS, WAXS, XPS, and FTIR exhibited distinct dose-dependent signatures. Because structural responses at neighboring length scales are closely coupled, these cross-scale correlations were used to construct a coherent mechanistic picture of the irradiation-induced structural evolution (Fig. 7b).

More decisively, both thermal post-cure and oxidation proceed monotonically with exposure: the former can only densify the network, and the latter is reflected in the strictly monotonic increase of the oxidized C 1s and O 1s components. Neither can account for the

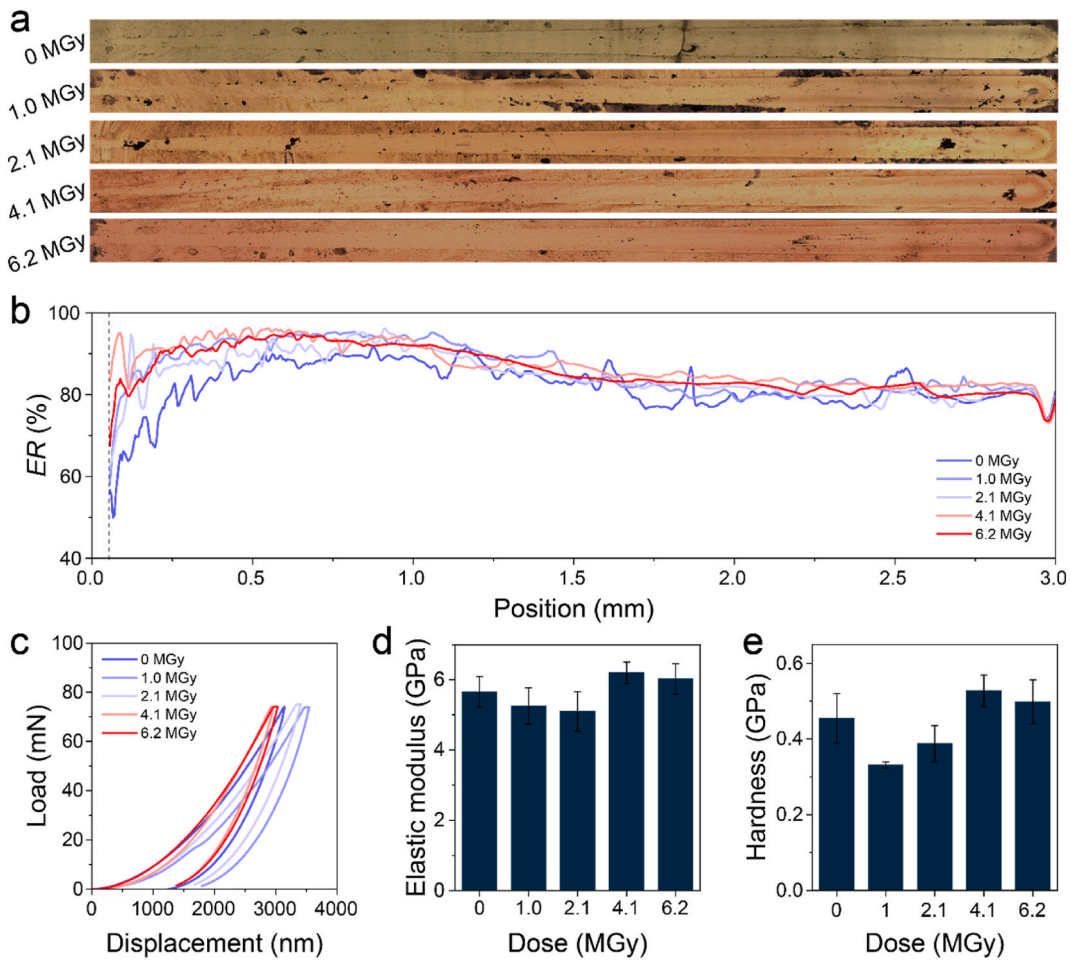

Fig. 6. Nanoindentation and microscratch mechanical characterization of CE resins as a function of absorbed dose. (a) Micrographs of microscratch tracks and (b) corresponding elastic recovery (ER) profiles along the scratch path. (c) Load-displacement curves, (d) elastic modulus, and (e) hardness values obtained from nanoindentation tests.

softening observed between 1.0 and 2.1 MGy, and a monotonic process cannot produce the nonmonotonic response reported here. It should also be noted that the techniques used differ in sampling depth: XPS (~10 nm), ATR-FTIR (~0.7–2 μm) and nanoindentation (3–3.5 μm contact depth) report near-surface behavior, whereas PALS and WAXS average over the full specimen thickness. The consistency of the transition dose across both groups indicates that the near-surface mechanical response tracks the underlying bulk structural evolution, and the two are treated here as complementary rather than equivalent measures.

In the low-dose regime of 0–2.1 MGy, neutron irradiation initially induced chemical alteration and partial cleavage of methylene and aromatic ether linkages within the polycyanurate network. These reactions were coupled to the generation and propagation of radical species. At the nanometer scale, disruption of these linkages loosened the CE network and expanded its free-volume structure. Although these changes produced little discernible microscale morphological damage, they resulted in deterioration of the local mechanical properties. In the high-dose regime, by contrast, radical recombination and secondary crosslinking became increasingly dominant, promoting the partial restoration of the linkages and subsequent network densification. The accompanying contraction of the free-volume structure was consistent with the recovery of the local mechanical properties. Collectively, this behavior can be defined as "molecular- and nanoscale-driven structural aging".

This two-regime behavior can be further understood by comparison with previous γ-irradiation studies of CE-based networks. Preferential degradation of ether-containing linkages has also been reported in γ-irradiated CE/epoxy networks [8], while CE/benzoxazine systems exhibited nonmonotonic mechanical and thermal responses, with initial deterioration followed by partial recovery or enhancement at intermediate doses [9]. These observations indicate that competition between bond degradation and radiation-induced network reorganization or additional crosslinking is not unique to neutron-containing irradiation fields. In the present CE system, however, the crossover was consistently resolved at approximately 2.1 MGy through correlated changes in free volume, molecular organization, chemical structure, and local mechanical properties.

A fundamental distinction lies in the mode of energy deposition. Whereas γ-rays interact predominantly through electromagnetic processes and transfer energy mainly through secondary electrons, neutrons interact directly with atomic nuclei and can deposit energy through recoil particles and nuclear reactions [58–60]. The neutron component therefore introduces additional energy-deposition pathways that are absent under γ-only irradiation. Although the present results do not isolate the individual neutron and γ contributions, these differences in radiation–matter interactions may contribute to the specific multiscale aging response observed here.

4. Conclusion

This study establishes a multiscale fingerprinting framework for identifying the dose-dependent aging of neutron-irradiated cyanate ester networks up to 6.2 MGy. The CE network exhibited two distinct regimes separated at approximately 2.1 MGy. At low doses, alteration of

a

Scale	Analysis	Regime 1 (Low-dose)	Regime 2 (High-dose)
Macroscopic/ microscopic	Optical imaging	Yellowing	Yellowing
	SEM	-[a]	-
Nano-/subnanoscale	PALS	Free volume expansion	Free volume contraction
	SAXS	-	-
	WAXS	-	Heterogeneous yet locally compact packing
Molecular/chemical	XPS	Progressive oxidation	Progressive oxidation with altered triazine-adjacent environments
	FTIR	Hydrogen abstraction and ether cleavage	Partial linkage restoration via radical recombination
Mechanical	Nanoindentation	Modulus reduction	Modulus recovery

[a]- No distinct regime-dependent change

b

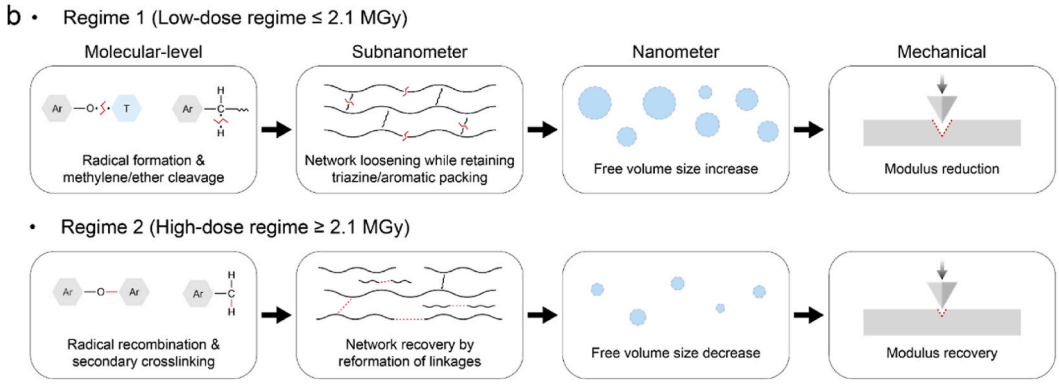

Fig. 7. Neutron-irradiation-induced degradation behavior of the cured CE network across multiple length scales. (a) Regime-dependent structural, chemical, and mechanical responses to irradiation. (b) Schematic illustration of the proposed two-regime degradation mechanism.

methylene and aromatic ether linkages caused network loosening, free-volume expansion, and deterioration of local mechanical properties. At higher doses, radical recombination and secondary crosslinking promoted network densification, free-volume contraction, and mechanical recovery. Notably, these changes occurred predominantly at the molecular and nano-/subnanometer scales without pronounced microscale morphological damage. These correlated signatures therefore define the irradiation response of CE as molecular- and nanoscale-driven structural aging and demonstrate the value of multiscale analysis for identifying hidden damage mechanisms and transition doses in radiation-resistant thermosetting networks. Such an approach may provide a useful basis for assessing irradiation-induced structural evolution before macroscopic failure becomes apparent and for improving durability evaluation of polymer networks in radiation-intensive environments. However, the present findings are limited to a specific CE system, irradiation condition, and discrete dose range. Further validation across different CE formulations, radiation types and exposure conditions, with finer dose resolution and long-term performance assessment, is required to establish the broader applicability of the observed transition behavior.

CRediT authorship contribution statement

Minjung Han: Writing – original draft, Visualization, Methodology, Data curation, Investigation. **Kisu Kim:** Writing – original draft, Visualization, Methodology, Investigation, Data curation. **Gyeongjun Kim:** Writing – original draft, Methodology, Investigation, Data curation, Visualization. **Youngsu Jeong:** Writing – original draft, Visualization, Methodology, Investigation. **Hyunjun Lee:** Formal analysis. **Wonjin Na:** Formal analysis. **Min Wook Lee:** Formal analysis. **Dae Han Sung:** Formal analysis. **Ki-Ho Nam:** Formal analysis. **Hyeonuk Yeo:** Formal analysis. **Jaegi Lee:** Writing – original draft, Supervision, Methodology, Conceptualization. **Hyeong Min Jin:** Writing – original draft, Supervision, Resources, Methodology, Conceptualization. **Youngho Eom:** Writing – review & editing, Writing – original draft, Supervision, Project administration, Conceptualization, Methodology.

Declaration of competing interest

The authors declare that they have no known competing financial interests or personal relationships that could have appeared to influence the work reported in this paper.

Acknowledgements

This work was supported by the National Research Foundation of Korea (NRF) grant funded by the Korea government (MSIT) (No. RS-2025-25442298). This research was also supported by the Nano & Material Technology Development Program through the National Research Foundation of Korea (NRF), funded by the Ministry of Science and ICT (RS-2026-25593128).

Appendix A. Supplementary data

Supplementary data to this article can be found online at https://doi.org/10.1016/j.polymertesting.2026.109381.

Data availability

Data will be made available on request.

References

[1] I. Hamerton (Ed.), Chemistry and Technology of Cyanate Ester Resins, Springer, Dordrecht, 1994, https://doi.org/10.1007/978-94-011-1326-7.

[2] A. Inamdar, J. Cherukattu, A. Anand, B. Kandasubramanian, Thermoplastic-toughened high-temperature cyanate esters and their application in advanced composites, Ind. Eng. Chem. Res. 57 (2018) 4479–4504, https://doi.org/10.1021/acs.iecr.7b05202.

[3] P. Bartolomeo, J.F. Chailan, J.L. Vernet, Curing of cyanate ester resin: a novel approach based on FTIR spectroscopy and comparison with other techniques, Eur. Polym. J. 37 (2001) 659–670, https://doi.org/10.1016/S0014-3057(00)00165-8.

[4] C.A. Fyfe, J. Niu, S.J. Rettig, N.E. Burlinson, High-resolution carbon-13 and nitrogen-15 NMR investigations of the mechanism of the curing reactions of cyanate-based polymer resins in solution and the solid state, Macromolecules 25 (1992) 6289–6301, https://doi.org/10.1021/ma00049a028.

[5] I.B. Recalde, D. Recalde, R. García-Lopera, C.M. Gómez, FTIR isothermal cure kinetics and morphology of dicyanate ester resin/polysulfone blends, Eur. Polym. J. 41 (2005) 2635–2643, https://doi.org/10.1016/j.eurpolymj.2005.05.027.

[6] C. Marieta, M. del Rio, I. Harismendy, I. Mondragon, Effect of the cure temperature on the morphology of a cyanate ester resin modified with a thermoplastic: characterization by atomic force microscopy, Eur. Polym. J. 36 (2000) 1445–1454, https://doi.org/10.1016/S0014-3057(99)00203-7.

[7] J. Li, Z. Wu, C. Huang, L. Li, Gamma irradiation effects on cyanate ester/epoxy insulation materials for superconducting magnets, Fusion Eng. Des. 89 (2014) 3112–3116, https://doi.org/10.1016/j.fusengdes.2014.09.012.

[8] A. Idesaki, H. Uechi, Y. Hakura, H. Kishi, Effects of gamma-ray irradiation on a cyanate ester/epoxy resin, Radiat. Phys. Chem. 98 (2014) 1–6, https://doi.org/10.1016/j.radphyschem.2013.12.032.

[9] A. Zegaoui, A.-R. Wang, A.Q. Dayo, B. Tian, W.-B. Liu, J. Wang, Y.-G. Liu, Effects of gamma irradiation on the mechanical and thermal properties of cyanate ester/benzoxazine resin, Radiat. Phys. Chem. 141 (2017) 110–117, https://doi.org/10.1016/j.radphyschem.2017.06.010.

[10] R.L. Clough, High-energy radiation and polymers: a review of commercial processes and emerging applications, Nucl. Instrum. Methods Phys. Res. B 185 (2001) 8–33, https://doi.org/10.1016/S0168-583X(01)00966-1.

[11] C.L. Moad, D.J. Winzor, Quantitative characterization of radiation degradation in polymers by evaluation of scission and cross-linking yields, Prog. Polym. Sci. 23 (1998) 759–813, https://doi.org/10.1016/S0079-6700(97)00041-5.

[12] M. Celina, E. Linde, D. Brunson, A. Quintana, N. Giron, Overview of accelerated aging and polymer degradation kinetics for combined radiation-thermal environments, Polym. Degrad. Stabil. 166 (2019) 353–378, https://doi.org/10.1016/j.polymdegradstab.2019.06.007.

[13] W. Lou, C. Xie, X. Guan, Understanding radiation-thermal aging of polydimethylsiloxane rubber through molecular dynamics simulation, npj Mater. Degrad. 6 (2022) 84, https://doi.org/10.1038/s41529-022-00299-1.

[14] Aleshka Nicolle Chinchay-Bengoa, Mary Flor Césare Coral, Edgar Catarí, Jorge Yarasca Huanacune, Jisennia Marleny Vara-Garcia, Astrid Herrera, Edward Longa, Javier Jorge Gago Campusano, Effect of Gamma Radiation on the Properties of Recycled High-Density Polyethylene Composites Reinforced with Pine and Bolaina Wood, Fibers and Polymers 27 (6) (2026) 2931–2945, https://doi.org/10.1007/s12221-026-01387-8. https://link.springer.com/10.1007/s12221-026-01387-8. (Accessed 24 March 2026).

[15] J. Davenas, I. Stevenson, N. Celette, S. Cambon, J.L. Gardette, A. Rivaton, L. Vignoud, Stability of polymers under ionising radiation: the many faces of radiation interactions with polymers, Nucl. Instrum. Methods Phys. Res. B 191 (2002) 653–661, https://doi.org/10.1016/S0168-583X(02)00628-6.

[16] A. Abdel Moez, S.S. Aly, Y.H. Elshaer, Effect of gamma radiation on low density polyethylene (LDPE) films: optical, dielectric and FTIR studies, Spectrochim. Acta Mol. Biomol. Spectrosc. 93 (2012) 203–207, https://doi.org/10.1016/j.saa.2012.02.031.

[17] A.S. Aliyu, S.M. Iorshase, L.J. Utume, E.O. Adamu, S. Muhammad, S.W. Oyeyemi, I. M. Saleh, Moderate gamma irradiation-induced property alterations and degradation in doum-fibre reinforced high-density polyethylene (dHDPE) composites, Radiat. Phys. Chem. 238 (2026) 113175, https://doi.org/10.1016/j.radphyschem.2025.113175.

[18] Y.-S. Chung, S.-H. Kim, S.-Y. Baek, K.-M. Sun, J.-H. Moon, K.-H. Lee, Characteristic examination of the HANARO pneumatic transfer irradiation system for a neutron activation analysis, in: Transactions of the Korean Nuclear Society Spring Meeting, Gyeongju, Korea, May 29–30, 2008, pp. 663–664.

[19] M.-S. Kim, S.-Y. Hwang, H.-S. Jung, K.-H. Lee, Measurements of nuclear heating rate and neutron flux in HANARO CN hole for designing the moderator cell of cold neutron source, in: Proceedings of the 2005 TRTR–IGORR Meeting, 2005, pp. 1–6. Gaithersburg, MD, USA.

[20] S. Tencé-Girault, S. Lebreton, O. Bunau, P. Dang, F. Bargain, Simultaneous SAXS-WAXS experiments on semi-crystalline polymers: example of PA11 and its brill transition, Crystals 9 (2019) 271, https://doi.org/10.3390/cryst9050271.

[21] J.H. Park, S. Jang, Y.N. Kim, J. Choi, H. Yeo, K.-H. Nam, High-temperature insulating polyimide aerogels with a hierarchical porous hyper-cross-linked structure derived from aqueous polymerization of mesostructured silica-grafted poly(amic acid) salt, Polym. Test. 147 (2025) 108797, https://doi.org/10.1016/j.polymertesting.2025.108797.

[22] S. Khim, Y.C. Hwang, J. Choi, H. Park, K.-H. Nam, Temperature-invariant large broadband polyimide dielectrics with multimodal porous networks, ACS Appl. Polym. Mater. 5 (2023) 4159–4169, https://doi.org/10.1021/acsapm.3c00369.

[23] J.V. Olsen, P. Kirkegaard, N.J. Pedersen, M. Eldrup, PALSfit: a new program for the evaluation of positron lifetime spectra, Phys. Status Solidi C 4 (2007) 4004–4006, https://doi.org/10.1002/pssc.200675868.

[24] G. Consolati, D. Nichetti, F. Quasso, Probing the free volume in polymers by means of positron annihilation lifetime spectroscopy, Polymers 15 (2023) 3128, https://doi.org/10.3390/polym15143128.

[25] S.J. Tao, Positronium annihilation in molecular substances, J. Chem. Phys. 56 (1972) 5499–5510, https://doi.org/10.1063/1.1677067.

[26] M. Eldrup, D. Lightbody, J.N. Sherwood, The temperature dependence of positron lifetimes in solid pivalic acid, Chem. Phys. 63 (1981) 51–58, https://doi.org/10.1016/0301-0104(81)80307-2.

[27] J. Tauc, R. Grigorovici, A. Vancu, Optical properties and electronic structure of amorphous germanium, Phys. Status Solidi B 15 (1966) 627–637, https://doi.org/10.1002/pssb.19660150224.

[28] J.-H. Choi, D.-K. Kim, C.-H. Jung, R. Ganesan, Preparation of patterned polymer brushes by radiation-induced grafting, J. Kor. Phys. Soc. 52 (2008) 880–883, https://doi.org/10.3938/jkps.52.880.

[29] C.-H. Jung, I.-T. Hwang, I.-S. Kuk, O.-S. Kwon, K. Shin, J.-H. Choi, Selective immobilization of silver nanoparticles onto poly(acrylic acid)-patterned poly (tetrafluoroethylene) surface prepared by using radiation-induced graft polymerization, J. Chem. Biol. Interfaces 1 (2013) 53–57.

[30] M. Kim, J. Seo, C. Park, J.H. Jeong, H.J. Kim, D.W. Chae, Y. Eom, 2D gradient and correlation FTIR analyses for optimizing thermal curing process of commercial-grade polyurethane coatings for automotive interior parts, Prog. Org. Coating 185 (2023) 107896, https://doi.org/10.1016/j.porgcoat.2023.107896.

[31] J.H. Jeong, J. Seo, M. Kim, C. Park, H.J. Kim, Y.H. Choi, H. Kim, Y. Eom, Rheology and FTIR-based tools for analyzing thermal-induced physical aging of polyurethane coatings for automotive interior plastic parts, Prog. Org. Coating 177 (2023) 107412, https://doi.org/10.1016/j.porgcoat.2023.107412.

[32] W.C. Oliver, G.M. Pharr, An improved technique for determining hardness and elastic modulus using load and displacement sensing indentation experiments, J. Mater. Res. 7 (1992) 1564–1583, https://doi.org/10.1557/JMR.1992.1564.

[33] W.C. Oliver, G.M. Pharr, Measurement of hardness and elastic modulus by instrumented indentation: advances in understanding and refinements to methodology, J. Mater. Res. 19 (2004) 3–20, https://doi.org/10.1557/jmr.2004.19.1.3.

[34] F. Hosni, K. Farah, H. Kaouach, A. Louati, R. Chtourou, A.H. Hamzaoui, Effect of gamma-irradiation on the colorimetric properties of epoxy-resin films: potential use in dosimetric application, Nucl. Instrum. Methods Phys. Res. B 311 (2013) 1–4, https://doi.org/10.1016/j.nimb.2013.06.003.

[35] F. Xie, L. Liu, X. Gong, L. Huang, J. Leng, Y. Liu, Effects of accelerated aging on thermal, mechanical and shape memory properties of cyanate-based shape memory polymer: i vacuum ultraviolet radiation, Polym. Degrad. Stabil. 138 (2017) 91–97, https://doi.org/10.1016/j.polymdegradstab.2017.03.001.

[36] R.L. Clough, G.M. Malone, K.T. Gillen, J.S. Wallace, M.B. Sinclair, Discoloration and subsequent recovery of optical polymers exposed to ionizing radiation, Polym. Degrad. Stabil. 49 (1995) 305–313, https://doi.org/10.1016/0141-3910(95)87013-X.

[37] R.L. Clough, K.T. Gillen, G.M. Malone, J.S. Wallace, Color formation in irradiated polymers, Radiat. Phys. Chem. 48 (1996) 583–594, https://doi.org/10.1016/0969-806X(96)00075-8.

[38] M. Abd El-Rahman, K.M. Yassien, A.A.M. Yassene, Effect of gamma irradiation on the optical properties of epoxy resin thin films, Optik 183 (2019) 962–970, https://doi.org/10.1016/j.ijleo.2018.12.182.

[39] E. Saion, Susilawati, A. Doyan, S. Zainal Abidin, Z. Azmi, A. Zulkfli, A.R. Mohd Zaki, K.Z.H. Dahlan, T. Karni, Changes in the optical band gap and absorption edge of gamma-irradiated polymer blends, J. Appl. Sci. 5 (2005) 1825–1829, https://doi.org/10.3923/jas.2005.1825.1829.

[40] A. Doyan, S. Susilawati, S. Prayogi, M.R. Bilad, M.F. Arif, N.M. Ismail, Polymer film blend of polyvinyl alcohol, trichloroethylene and cresol red for gamma radiation dosimetry, Polymers 13 (2021) 1866, https://doi.org/10.3390/polym13111866.

[41] L. Zheng, J. Wang, J. Li, Y. Zhang, K. Li, Y. Wei, Preparation, evaluation and modification of PVDF-CTFE hydrophobic membrane for MD desalination application, Desalination 402 (2017) 162–172, https://doi.org/10.1016/j.desal.2016.10.003.

[42] S. Banerjee, R. Yang, C.E. Courchene, T.E. Conners, Scanning electron microscopy measurements of the surface roughness of paper, Ind. Eng. Chem. Res. 48 (2009) 4322–4325, https://doi.org/10.1021/ie900029v.

[43] B.A. Banks, K.K. de Groh, S.K. Miller, Low Earth orbital atomic oxygen interactions with spacecraft materials, MRS Proc 851 (2004), https://doi.org/10.1557/PROC-851-NN8.1. NN8.1.

[44] A. Chapiro, General consideration of the radiation chemistry of polymers, Nucl. Instrum. Methods Phys. Res. B 105 (1995) 5–7, https://doi.org/10.1016/0168-583X(95)00861-6.

[45] C.V. More, H. Alavian, P.P. Pawar, Evaluation of gamma ray and neutron attenuation capability of thermoplastic polymers, Appl. Radiat. Isot. 176 (2021) 109884, https://doi.org/10.1016/j.apradiso.2021.109884.

[46] M. Zeng, C. Lu, B. Wang, C. Qi, Free volume hole size of cyanate ester resin/epoxy resin interpenetrating networks and its correlations with physical properties, Radiat. Phys. Chem. 79 (2010) 966–975, https://doi.org/10.1016/j.radphyschem.2010.03.006.

[47] H.S. Hussain, Structure dependence of gamma ray irradiation effects on polyurethane and epoxy resin studied by PAL technique, Iraqi J. Phys. 13 (2015) 157–163, https://doi.org/10.30723/ijp.v13i27.274.
[48] R.L. Miller, R.F. Boyer, Regularities in x-ray scattering patterns from amorphous polymers, J. Polym. Sci. Polym. Phys. Ed. 22 (1984) 2043–2050, https://doi.org/10.1002/pol.1984.180221204.
[49] M.-H. Kim, J.D. Londono, A. Habenschuss, Structure of molten stereoregular polyolefins with different side-chain sizes: Linear polyethylene, polypropylene, poly(1-butene), and poly(4-methyl-1-pentene), J. Polym. Sci. B Polym. Phys. 38 (2000) 2480–2485, https://doi.org/10.1002/1099-0488(20000915)38:18%3C2480::AID-POLB150%3E3.0.CO;2-8.
[50] A. Rahnamoun, D.P. Engelhart, S. Humagain, H. Koerner, E. Plis, W.J. Kennedy, R. Cooper, S.G. Greenbaum, R. Hoffmann, A.C.T. van Duin, Chemical dynamics characteristics of Kapton polyimide damaged by electron beam irradiation, Polymer 176 (2019) 135–145, https://doi.org/10.1016/j.polymer.2019.05.035.
[51] L. Wang, F. Zhang, Y. Liu, S. Du, J. Leng, Thermal, mechanical and shape fixity behaviors of shape memory cyanate under γ-ray radiation, Smart Mater. Struct. 31 (2022) 045010, https://doi.org/10.1088/1361-665X/ac5538.
[52] D. Peng, Z. Han, The effect of electron radiation on POSS/cyanate ester nanocomposites, Vacuum 215 (2023) 112360, https://doi.org/10.1016/j.vacuum.2023.112360.
[53] M.L. Ramirez, R. Walters, R.E. Lyon, E.P. Savitski, Thermal decomposition of cyanate ester resins, Polym. Degrad. Stabil. 78 (2002) 73–82, https://doi.org/10.1016/S0141-3910(02)00121-0.
[54] M.Y. Rivera Lopez, A. Suliga, F. Scarpa, I. Hamerton, Development of cyanate ester-oligosiloxane copolymers for deployable satellite applications, Polymer 290 (2024) 126573, https://doi.org/10.1016/j.polymer.2023.126573.
[55] U. Szeluga, B. Kumanek, S. Pusz, S. Czajkowska, Preparation and characterization of carbon foams derived from cyanate esters and cyanate/epoxy copolymers, J. Therm. Anal. Calorim. 122 (2015) 271–279, https://doi.org/10.1007/s10973-015-4730-x.
[56] K. Nakamura, S. Ogata, Y. Ikada, Assessment of heat and storage conditions on γ-ray and electron beam irradiated UHMWPE by electron spin resonance, Biomaterials 19 (1998) 2341–2346, https://doi.org/10.1016/S0142-9612(98)00150-1.
[57] A. Charlesby, D. Libby, M.G. Ormerod, Radiation damage in polyethylene as studied by electron spin resonance, Proc. R. Soc. Lond. A Math. Phys. Sci. 262 (1961) 207–218, https://doi.org/10.1098/rspa.1961.0113.
[58] P.J. Karpius, T.D. Reilly, Gamma-Ray interactions with matter, in: W.H. Geist, P. A. Santi, M.T. Swinhoe (Eds.), Nondestructive Assay of Nuclear Materials for Safeguards and Security, Springer Nature Switzerland, Cham, 2024, pp. 27–41, https://doi.org/10.1007/978-3-031-58277-6_3.
[59] M.T. Swinhoe, J.D. Hutchinson, P.M. Rinard, Neutron interactions with matter, in: W.H. Geist, P.A. Santi, M.T. Swinhoe (Eds.), Nondestructive Assay of Nuclear Materials for Safeguards and Security, Springer Nature Switzerland, Cham, 2024, pp. 307–323, https://doi.org/10.1007/978-3-031-58277-6_14.
[60] A. Musumarra, F. Leone, C. Massimi, M.G. Pellegriti, F. Romano, R. Spighi, M. Villa, RIPTIDE: a novel recoil-proton track imaging detector for fast neutrons, J. Instrum. 16 (2021) C12013, https://doi.org/10.1088/1748-0221/16/12/C12013.